

Experimental determination of Lamb wave dispersion diagrams over large frequency ranges in fiber metal laminates

Tilman Barth^{a,*}, Johannes Wiedemann^b, Thomas Roloff^b, Tim Behrens^b, Natalie Rauter^a, Christian Hühne^{b,c}, Michael Sinapius^b and Rolf Lammering^a

^a*Helmut-Schmidt-University / University of the Federal Armed Forces Hamburg, Institute of Mechanics, Holstenhofweg 85, Hamburg, 22043, Germany*

^b*TU Braunschweig, Institute of Mechanics and Adaptronics, Langer Kamp 6, Braunschweig, 38106, Germany*

^c*DLR, Institute of Composite Structures and Adaptive Systems, Lilienthalplatz 7, Braunschweig, 38108, Germany*

ABSTRACT

Fiber metal laminates (FML) are of high interest for lightweight structures as they combine the advantageous material properties of metals and fiber-reinforced polymers. However, low-velocity impacts can lead to complex internal damage. Therefore, structural health monitoring (SHM) with guided ultrasonic waves, in this case, referred to as Lamb waves, is an approach to identify such damage. Numerical simulations form the basis for corresponding investigations, but experimental validation of propagation diagrams over a wide frequency range is hardly found in the literature. In this work the dispersive relation of Lamb waves is experimentally determined for an FML made of carbon fiber-reinforced polymer and steel. For this purpose, a multi-frequency excitation is used to generate Lamb waves and the resulting wave field is measured via laser scanning vibrometry. The data are processed by means of a non-uniform discrete 2d Fourier transform and analyzed in the frequency-wavenumber domain. The experimental data are in good agreement with data from a numerical solution of the analytical framework. In conclusion, this work presents a highly automatable method to experimentally determine dispersion diagrams of Lamb waves in FML over large frequency ranges with high accuracy and reproducibility.

1. Introduction

Fiber metal laminates (FML) are advanced material systems for aeronautic applications since they show superior performance over aerospace-grade aluminum and higher ductility compared to fiber-reinforced polymers (FRP) [1, 2]. However, due to their layered structure, low-velocity impacts can create internal damage in the material that is barely visible from the outside [3–5]. Therefore, the approach of using sensors to assess the current "health" state of the component at any time during the life cycle is particularly interesting for FML applications [6, 7].

To detect damage in thin-walled components through structural health monitoring (SHM) systems, the use of guided ultrasonic waves (GUW) has been of major interest in research [8–10]. GUW can travel over large distances in thin solid structures without dissipating much energy and show interactions with inhomogeneities such as damage [10] and are therefore particularly well-suited for this kind of application.

FML specimens exhibit strong, abrupt changes in material properties across the specimen thickness. Therefore, the question arises whether the GUW's occurring in these material systems can be calculated using the methods developed for isotropic waveguides and extended for fiber composites, cf. [11, 12]. A first indication that the respective methods can be applied is shown by Pant et al. [13]. Therein a 3d linear elasticity model is developed to determine the dispersion diagrams and displacement fields of Lamb waves in monoclinic and higher-order symmetric materials such as FML. To validate the performance of the method, GLARE3-3/4 is investigated numerically and experimentally. Using a combination of one actuator and two sensors, the group and phase velocities for the fundamental wave modes are extracted. The setup allowed an experimental validation of the numerical results for the fundamental modes. However, the A_0 group velocity was validated in another frequency range than the S_0 phase velocity. Since the

*Corresponding author

✉ barth@hsu-hh.de (T. Barth)

ORCID(s): 0000-0002-0667-0609 (T. Barth); 0000-0003-2040-0143 (J. Wiedemann); 0000-0002-8834-710X (T. Roloff); 0000-0002-4493-445X (T. Behrens); 0000-0003-1704-1426 (N. Rauter); 0000-0002-2218-1223 (C. Hühne); 0000-0002-1873-9140 (M. Sinapius); 0000-0002-0867-1859 (R. Lammering)

physical phenomena of guided waves in complex material systems are comparable to those of Lamb waves in isotropic waveguides, the waves studied in this work are also referred to as Lamb waves.

Beyond that, only little literature can be found that addresses the wave propagation in FMLs and especially literature targeting experimental investigations is rare. Maghsoodi et al. [14] address damage detection methods with Lamb waves using phased arrays in FML numerically. The validation is done using ABAQUS and the transfer matrix method at a single frequency of 100 kHz. Another investigation by Muc et al. [15] addresses the numerical determination of dispersion diagrams in FML using the stiffness matrix method and FEM. Laminates made of aluminum and carbon fiber-reinforced polymer (CFRP) as well as aluminum and glass fiber reinforced polymer (GFRP) are investigated. The numerical results for the group velocity are experimentally validated using two distinct sensors to determine the time-of-flight of a single A_0 -mode wave package at 100 kHz. Tai et. al. [16] are modeling the Lamb wave propagation in FML numerically to investigate the effect of defects. An experimental setup is used to determine the group velocity for validating the numerical model. However, only a small frequency range of 50-250 kHz with a large step size of 25 kHz is investigated for the A_0 -mode. Gao et al. [17] are using a combination of the state-vector formalism and the Legendre polynomials to simulate the Lamb wave propagation in multi-layered anisotropic composite laminates. Apart from isotropic, quasi-isotropic, and anisotropic materials, the aluminum/GFRP combination standard GLARE3-3/2 is investigated. The results show a good fit with the global matrix method over a broad frequency range. However, the results are not validated experimentally. In addition, investigations on structures with metal and FRP interfaces exist. Attar et al. [18] perform dispersion curve measurements on the adhesive bond between aluminum and CFRP using an impulse excitation for broadband Lamb wave measurements. The experimental results match with the simulations. However, the impulse excitation is not suited to investigate a specific frequency band. LeCrom et al. [19] investigate the bonding layer between an aluminum structure and an applied CFRP patch using a laser scanning vibrometer (LSV). They determine dispersion curves for SH -waves and an isotropic structure with an anisotropic patch. However the focus of these investigations is on the characterization of bonding interfaces between those two materials with an additional bonding layer (0.2-0.5 mm) out of pure epoxy resin. The different layers of FMLs as considered within the scope of this work on the other hand are bonded during a one-step manufacturing process without any additional adhesive. Hence, an explicit bonding layer is not found in FMLs and the results presented above are not directly transferable to the FML material in this work.

The state of the research shows that there is a significant need for accurate experimental Lamb wave dispersion measurements in FML. This publication aims on closing this gap by providing a highly automatable method and consequently experimentally determined dispersion diagrams for FML over a large frequency range with a high resolution. Therefore, a method [20] proposed by the authors that has already shown very good results in isotropic materials, is extended to FML. It is based on the use of 2d Fourier transformations to evaluate the measurement data of Lamb waves which has already successfully been done for example by [21–23] for isotropic materials. To do so, the displacements of the material points on the surface of the specimens is measured with the use of a LSV. Time signals are recorded at points along a measuring path in the direction of the wave propagation to generate data depending on time and space. The data is evaluated by means of a non-uniform 2d Discrete Fourier Transform (2d-DFT) [24]. This method is specially tuned to increase the accuracy of the measurements as much as possible by the use of multi-frequency excitation signals instead of impulse excitations, while still enabling high automation and thus the possibility to cover large frequency ranges.

The measurements are performed from three different points of view. Firstly, they are intended to provide experimental dispersion relations for FML structures over large frequency ranges to fill a gap existing in the literature. Secondly, they aim at showing the applicability of the used method in non-isotropic and inhomogeneous materials, in particular when the material properties exhibit large step changes across the thickness. For this purpose, repeated measurements with different measurement setups at different locations are reviewed regarding their reproducibility. Thirdly, the suitability of strip specimens with a surface area of 110×490 mm is compared to square plate specimens with an edge length of 500 mm for this kind of application. This is done in preparation for follow-up work, as strip specimens enable a cost-effective alternative to plate specimens and fulfill the boundary conditions of future investigations.

The work presented here is structured as follows: After a short introduction to FMLs, the basics for the analytical description of waves in laminate structures are discussed. This is followed by the description of the experimental setups as well as the definition of the materials and specimens used in this work. Subsequently, the data generation, as well as the postprocessing, is discussed in detail. To show the performance of the presented experimental approach, several different investigations are addressed in the results section. First, the reproducibility of the measurements is

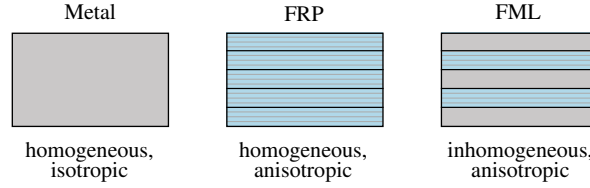


Figure 1: FMLs compared to other structural materials in terms of homogeneity of the material and direction dependent behavior.

discussed, followed by a comparison of different experimental setups in different locations. Furthermore, the influence of specimen size is evaluated. Finally, the measured dispersion relations are compared to numerically derived values of the analytic framework.

2. Background

2.1. Fiber metal laminates

FML aim at combining the advantages of metals, such as ductility, with the advantages of FRP, such as high specific properties [1, 25]. In FML, the metal is integrated into the fiber laminate in the form of thin sheets, which results in the ability to stop or bridge cracks. Thereby, a high damage tolerance is achieved [3, 26]. Moreover, advantages can be taken of the combination of the two materials e.g. for crash [27] or load-bearing applications [28, 29], as well as for function integration [30] and structure robustness [31]. Despite these advantages, low-velocity impact damages can lead to internal failure of the laminate, e.g. delaminations, which will be barely visible from the outside [3, 4]. This promotes the use of SHM methods that are also sensitive to internal defects [32].

The combination of metal and FRP in a layered composite results in a material system that is highly inhomogeneous and behaves in a very anisotropic manner [2, 33]. Figure 1 illustrates the subdivision of the different material systems according to their internal structure and directional behavior. The layered structure of the FML with its high impedance differences and interfaces between the two materials in the thickness direction is assumed to have a significant influence on the propagation of Lamb waves. The focus in this work will be on an FML consisting of CFRP and steel.

2.2. Waves in laminate structures

To describe the propagation of GUW in layered structures, the equation of motion must be solved with respect to stress-free boundary conditions at the surfaces of thin-walled structures. The fundamental relations that are used to derive the equation of motion are the balance of momentum

$$\text{Div } \boldsymbol{\sigma} + \rho_0 \mathbf{b} = \rho_0 \ddot{\mathbf{u}}, \quad (1)$$

the linear Green-Lagrange strain tensor

$$\mathbf{E} = \frac{1}{2} (\text{Grad}^T \mathbf{u} + \text{Grad } \mathbf{u}) \quad (2)$$

and Hooke's law

$$\boldsymbol{\sigma} = \mathbb{C} : \mathbf{E}. \quad (3)$$

Here, ρ_0 is the density, \mathbf{b} the body force density, \mathbf{u} the displacement field, $\boldsymbol{\sigma}$ the Cauchy stress tensor, and \mathbb{C} gives the stiffness tensor. Introducing Hooke's law in combination with the linear Green-Lagrange strain tensor into the balance of momentum and neglecting the volume forces leads to the well-known equation of motion, which is given for anisotropic materials by

$$\text{Div} (\mathbb{C} : \text{Grad } \mathbf{u}) - \rho_0 \ddot{\mathbf{u}} = \mathbf{0}. \quad (4)$$

Solving these differential equations for stress-free boundary condition by using the approach

$$\mathbf{u} = A \mathbf{p} e^{i(\mathbf{k} \cdot \mathbf{x} - \omega t)}, \quad (5)$$

with the polarization vector \mathbf{p} , the wavenumber vector \mathbf{k} , the angular frequency ω , the amplitude A , the spatial coordinates \mathbf{x} and the time t leads to the dispersion relation of GUW in thin-walled structures for a single material layer [34]

$$ik \begin{bmatrix} D_{ij}^+ & D_{il}^- H_{jl} \\ D_{il}^+ H_{jl} & D_{ij}^- \end{bmatrix} \begin{bmatrix} A_l^+ \\ A_l^- \end{bmatrix} e^{i(kx_l - \omega t)} = \begin{bmatrix} 0 \\ 0 \end{bmatrix} \quad (6)$$

with

$$D_{ij}^\pm = [(d_i^\pm)_1 \quad (d_i^\pm)_2 \quad (d_i^\pm)_3], \quad H_{ij} = \begin{bmatrix} e^{ik\alpha_1 h} & 0 & 0 \\ 0 & e^{ik\alpha_2 h} & 0 \\ 0 & 0 & e^{ik\alpha_3 h} \end{bmatrix}, \text{ and } A_j^\pm = [A_1^\pm \quad A_2^\pm \quad A_3^\pm]^T. \quad (7)$$

Here, h is the plate thickness, α_i are the eigenvalues of the Christoffel equation, and d_i^\pm can be calculated from

$$(d_i^\pm)_n = C_{i3kl} n_l^\pm (p_k)_n^\pm. \quad (8)$$

To be able to derive dispersion diagrams for laminates, information about the layered structure must be included into the dispersion relation. A comprehensive overview of methods for dispersion diagrams in layered structures is provided in Lowe [35]. Two common approaches are the transfer-matrix method [36–38] and the global matrix method [39]. The major drawback of the transfer-matrix method is its instability for large frequency-thickness pairs. This was later solved by Kausel [40], Wang [41], and Rokhlin [34, 42]. In contrast to this, the global matrix method is always stable and is therefore, used here to formulate the analytical framework that can be solved numerically to determine dispersion diagrams for the propagation of GUW in FML.

Within the global matrix method, the presented dispersion relations for single layers are connected by introducing a continuity condition for the displacements and stresses at the layer interfaces. Therefore, in accordance with Eq. (6), the displacements and out-of-plane stress components are collected in one system of equations. Following the matrix definitions in Eq. (7) and adding the displacement components leads to

$$\begin{bmatrix} u_1 \\ u_2 \\ u_3 \\ \sigma_{13}^* \\ \sigma_{23}^* \\ \sigma_{33}^* \end{bmatrix} = \begin{bmatrix} p_{11}^+ & p_{11}^- & p_{12}^+ & p_{12}^- & p_{13}^+ & p_{13}^- \\ p_{21}^+ & p_{21}^- & p_{22}^+ & p_{22}^- & p_{23}^+ & p_{23}^- \\ p_{31}^+ & p_{31}^- & p_{32}^+ & p_{32}^- & p_{33}^+ & p_{33}^- \\ d_{11}^+ & d_{11}^- & d_{12}^+ & d_{12}^- & d_{13}^+ & d_{13}^- \\ d_{21}^+ & d_{21}^- & d_{22}^+ & d_{22}^- & d_{23}^+ & d_{23}^- \\ d_{31}^+ & d_{31}^- & d_{32}^+ & d_{32}^- & d_{33}^+ & d_{33}^- \end{bmatrix} \text{diag} e^{i(\pm k\alpha_i h)} \begin{bmatrix} A_1^+ \\ A_1^- \\ A_2^+ \\ A_2^- \\ A_3^+ \\ A_3^- \end{bmatrix} \quad (9)$$

with $\sigma_{i3}^* = \frac{\sigma_{i3}}{ik}$. For a single layer n this is written in compact form as

$$\mathbf{U}_n = \mathbf{G}_n \mathbf{H}_n \mathbf{A}_n. \quad (10)$$

With this framework at hand, the continuity condition for the stresses and displacements at the layer interfaces

$$\mathbf{U}_n^+ - \mathbf{U}_{n+1}^- = 0, \quad (11)$$

where \mathbf{U}_n^+ gives the values at the upper surface of the layer n and \mathbf{U}_{n+1}^- at the lower surface of the layer $n+1$, respectively, provides the dispersion relation for GUW in layered structures like FML

$$\begin{vmatrix} [\mathbf{G}_{(N)} \mathbf{H}_{(N)}^+]_{4-6} & 0 \\ \mathbf{G}_{(N)} \mathbf{H}_{(N)}^- & -\mathbf{G}_{(N-1)} \mathbf{H}_{(N-1)}^+ \\ & \ddots \\ & \mathbf{G}_{(2)} \mathbf{H}_{(2)}^- & -\mathbf{G}_{(1)} \mathbf{H}_{(1)}^+ \\ 0 & \mathbf{G}_{(1)} \mathbf{H}_{(1)}^+]_{4-6} \end{vmatrix} = 0 \quad (12)$$

The subscript 4 – 6 refers to lines 4 to 6 of Eq. (10), which give the stress-free boundary conditions at the upper and lower edge of the layered structure.

It is important to note that there is no closed solution for this analytical framework. Thus, the computation of dispersion diagrams is based on an iterative procedure utilizing the bisection method. Even though the results are obtained numerically it is referred to as analytical solution in contrast to a purely numerical solution based on the FEM.

3. Experimental setup

In this section, the experimental realization used in this paper is presented. This includes the explanation of two different experimental setups (ES1 and ES2), the specifications and manufacturing of the specimens as well as the data acquisition and the postprocessing procedure.

3.1. Equipment and setup

The experimental setup aims at measuring the velocity of the material points at the specimen's surface along the wave propagation direction using a full-field laser scanning vibrometer (LSV), cf. [20, 32, 43, 44]. A piezoelectric actuator is used to generate the Lamb waves.

Figure 2 shows a schematic representation of the setup. A computer in combination with a signal generator provides the excitation signal presented in Section 3.3. The excitation signal is amplified using a high-voltage (HV) amplifier to drive the actuator that is adhered to the FML specimen. A detailed description of the specimens used is given in Section 3.2. The specimen's are mounted vertically in a way that no clamping on the vertical edges takes place and that an upright position is ensured at all times. Retroreflective tape is applied along the measurement path to increase the received signal amplitude by the LSV. Furthermore, a perpendicular alignment of the laser beam to the center of the measurement path is ensured. Taking into account the laser specifications, the horizontal distance between the LSV and the specimen is selected in such a way that both, the highest possible laser intensity can be measured and the spatial sampling along the measuring path is as high as possible. The velocities at the specimen's surface are acquired using a signal recorder and post-processed with the computer. Due to the positioning and orientation of the LSV, almost exclusively the out-of-plane component of the wave velocities is measured.

In the context of data transfer in research cooperations such as the authors' research unit who work at different institutes, and general applicability of the method under investigation, the question arises, whether it works independently of the setup. The method is assumed to perform with different setup specifications as long as the temporal and spatial resolutions, as well as the measuring lengths and durations, correspond to the signal processing requirements. Therefore, the measurements were carried out using two setups with the same architecture but different hardware. The two experimental setups are depicted in Figure 3 (ES1) and Figure 4 (ES2), respectively. A description of the hardware of the different setups is presented in Table 1. The decisive differences between the two measurement setups for this application are the sampling rate of the signal generators and the accuracy of the angular resolution of the LSVs used. The signal generator in ES2 has a maximum sampling rate of 1 MHz which, according to Shannon [45], results in a maximum excitation frequency of 0.5 MHz, whereas for ES1 a much higher excitation frequency of 62.5 MHz is theoretically possible. In the context of this work, a maximum excitation frequency of 1 MHz is used for ES1. Further, the accuracy of the angular resolution in ES2, affects the accuracy of signals with high wavenumbers. The resulting influence is discussed in Section 4.1.

3.2. Materials and specimen manufacturing process

The specimens in this work are made of alternating layers of CFRP prepreg (Hexcel Hexply 8552-AS4) and thin steel foils (1.4310) with a tensile strength of 1100-1200 MPa. Table 2 presents the material properties of the CFRP prepreg from different literature sources. The properties from NCAMP [46] are best documented in terms of experimental procedures and test results. However, the tests were performed with a prepreg material with a higher fiber area weight and a slightly different fiber volume content compared to the data sheet [47] of the prepreg at hand. In Garstka [48] the value of G_{23} is given equal to G_{12} and G_{13} which is not in accordance to the rules for transversal isotropic materials. Therefore, the value of G_{23} is questionable. Hörberg [49] gives the same values but with an updated G_{23} . However, the material is not specified by the authors but is assumed to be Hexcel 8552-AS4 due to the agreement of the other values. Johnston [50] gives the most comprehensive set of parameters with a fiber volume content similar to the data sheet of the material in this work. However, the tensile modulus in fiber direction shows around 10% difference to the values in other literature sources. In Section 4.5 the dispersion relations are calculated for the material data from [49] and [50] to account for the uncertainties in the material parameters. The material properties for the stainless steel alloy 1.4310 are given in Tabel 3. Own tensile tests of the steel foil show slightly higher values for the Young's modulus compared to the values provided by the DIN norm [51].

The process for the specimen production is a standard process for FMLs with fiber layers from prepreg systems. To assure a high interlaminar bonding strength between the different FML layers, the steel is mechanically pretreated with a vacuum suction blasting process. This process is beneficial for thin materials that would be damaged by classic sandblasting [52]. After the mechanical treatment, the surface is chemically cleaned with heptane. Subsequently, an

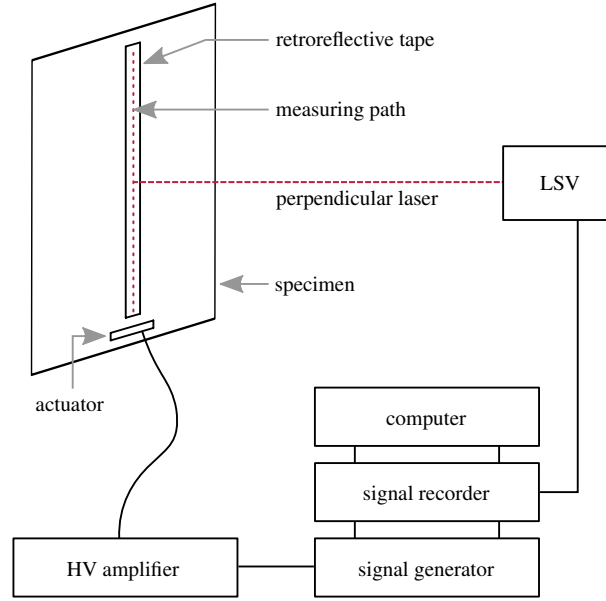


Figure 2: Schematic representation of the experimental setup.

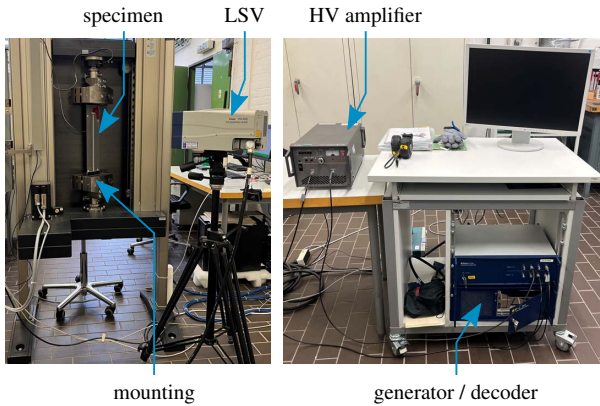


Figure 3: Experimental setup 1 (ES1)

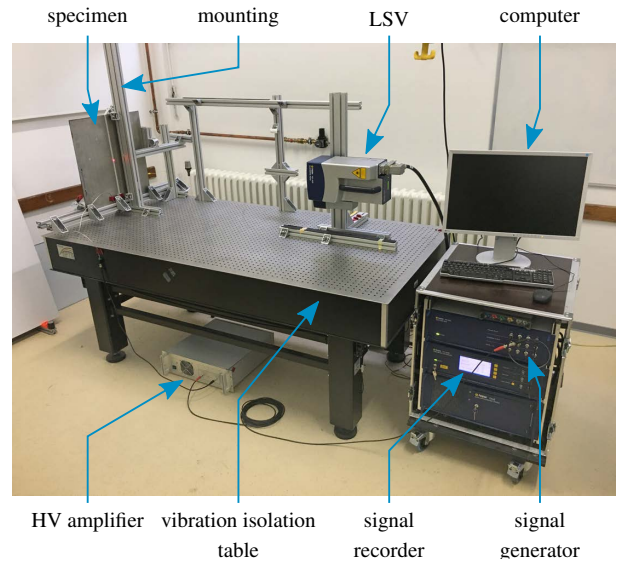


Figure 4: Experimental setup 2 (ES2)

aqueous sol-gel solution (3M Surface Pre-Treatment AC-130-2 [53]) is applied to all metal surfaces. The sol-gel layers increase the adhesive strength between CFRP and metal and lead to high interlaminar shear strength of the FML. The metal foil is dried for one hour after the sol-gel application and laminated immediately together with the CFRP prepreg layers [54, 55].

To cure the FML, the standard manufacturer-recommended autoclave process as found in the CFRP datasheet [47] is used. The process consists of a dwell stage at 110 °C and a final cure temperature of 180 °C.

Each specimen consists of 4 metal layers and 12 CFRP layers that are placed in a symmetric layup with two metal layers at the top and bottom of the specimen. In laminate notation, the layup can be described as $[St/0_4/St/0_2]_S$.

Device and parameter	ES1	ES2	Unit
Vibrometer			
Manufacturer	Polytec	Polytec	-
Model	PSV-500	PSV-400	-
angular resolution	< 0.001	0.002	°
Used working distance	≈ 535	≈ 1330	mm
Signal generator			
Manufacturer	Polytec	Polytec	-
Bandwidth	30	0.5	MHz
No. of sampling points	1×10^6	0.13×10^6	-
Max. sampling rate	125	1	MHz
Used sampling rate	10	1	MHz
Signal recorder			
Manufacturer	Polytec	Polytec	-
Sampling frequency	3.125	2.56	MHz
Used resolution	16	12	bit
Used amplitude range	100	20	mm/s/V

Table 1: Comparison of hardware specifications used in ES1 and ES2.

Value	Unit	Hexcel Hexply 8552-AS4				
		NCAMP [46]	Garstka [48]	Hörberg [49]	Johnston [50]	Data sheet [47]
E_1	GPa	132	135	135	122	141
$E_2 = E_3$	GPa	9.2	9.5	9.5	9.9	10
$G_{12} = G_{13}$	GPa	4.8	4.9	4.9	5.2	-
G_{23}	GPa	-	(4.9) ^a	3.3	3.4	-
$\nu_{12} = \nu_{13}$	-	0.3	0.3	0.3	0.27	-
$\nu_{23} = \frac{E_2}{2G_{23}} - 1$	-	-	0.45	0.45	0.47	-
f. vol. content	%	60.38	57.4	-	57.3	57.42
f. area weight	g m ⁻²	190	-	-	-	134
ρ	g cm ⁻³	1.57-1.60	-	-	-	1.58
t_{ply} (cured)	mm	0.19	-	0.13	-	0.13

^a not in accordance with rules of transversal isotropy**Table 2:** Comparison of material properties for the used prepreg material Hexcel Hexply 8552-AS4 from literature.

Value	Unit	Steel 1.4310 (X10CrNi18-8)	
		DIN EN 10151 [51]	own pretests
E	GPa	179	191
G	GPa	68.8 ^a	73.5 ^a
ν	-	0.3	0.3
t_{ply}	mm	0.12	0.12

^a calculated for linear elastic isotropic materials: $G = \frac{E}{2(1+\nu)}$ **Table 3:** Material properties for the austenitic steel alloy 1.4310 (X10CrNi18-8).

With the single-ply thicknesses from Table 2 and 3, this layup results in a nominal laminate thickness of 2.04 mm and a metal volume fraction (MVF) of 24 %. The layup and specimen architecture are schematically illustrated in Figure 5.

In this work, two types of specimen geometries are investigated, which mainly differ in their dimensions. One is strip-shaped, the other has the shape of a square plate. The dimensions of the specimens as well as the length of the measuring paths are given in Table 4.

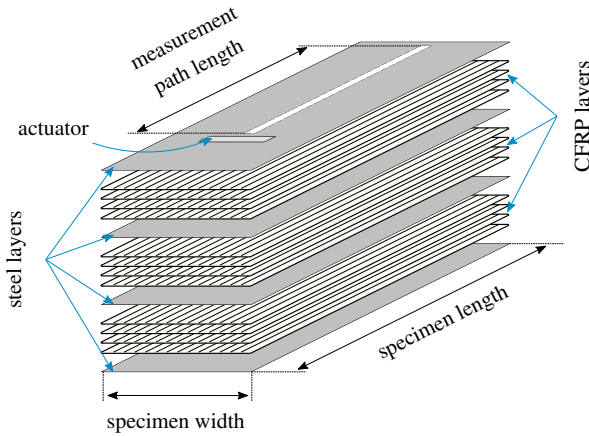


Figure 5: Schematic representation of the specimen architecture.

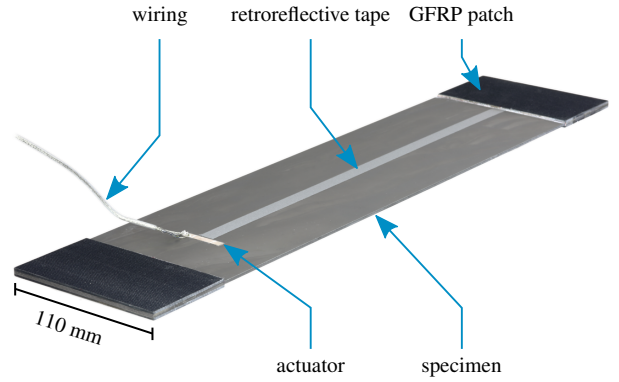


Figure 6: Photo of the used strip specimen.

A strip specimen with actuator and retroreflective tape is depicted in Figure 6. It is additionally equipped with patches of GFRP at the ends outside of the measuring path for future tests in a tensile testing machine. In order to reduce the influence of occurring edge reflections, the strip is additionally equipped on both sides with an energy dissipating butyl rubber tape along the edges. As the plate specimen is not equipped with GFRP patches, the available measurement path length is larger compared to the strip specimen. This is exploited in the measurements in ES2 to increase the quality of the measurements. In ES1, however, the measuring length for the plate specimen is reduced to the maximum path length of the strip specimen. This provides better comparability between the measurements of the two specimen types. For the actuation, a rectangular piezoceramic actuator with a length of 30 mm, a width of 5 mm and a ceramic thickness of 0.1 mm is used as the rectangular shape results in a more straight wavefront along the measuring path. The actuator contains a wrap-around electrode for single-sided access of the wiring. It is bonded to the specimen with Loctite EA9466 [56], which was cured under a vacuum bag to ensure a homogeneous thickness of the adhesive layer.

	Strip [mm]	Plate [mm]
Specimen length	490	500
Specimen width	110	500
Measurement path length ES1	320	320
Measurement path length ES2	320	450

Table 4: Geometry and measurement path length of the two investigated specimens.

Since the laminate thickness is a crucial parameter for the subsequent calculation of the Lamb wave propagation, the thickness for each of the specimens was measured after manufacturing at 10 evenly distributed points over the specimen's surface. Table 5 shows the results. Only minor deviations to the nominal thickness of 2.04 mm can be found.

	Strip [mm]	Plate [mm]
Mean thickness	2.031	2.046
Standard deviation	0.003	0.014

Table 5: Mean values resulting from thickness evaluations at 10 evenly distributed points over the specimen's surface for the plate and strip specimen.

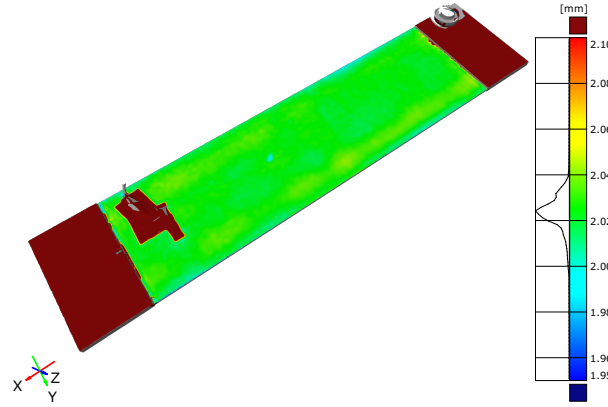


Figure 7: Thickness evaluation of strip specimen with GOM ATOS.

To additionally check for the homogeneity of the specimen's thickness, a three-dimensional measurement of the strip specimen was performed with an industrial 3D scanner (GOM ATOS). A surface model of the scanned object is generated from the measured point cloud and the thickness is evaluated. The result of this evaluation is shown in Figure 7. The measurement shows that the thickness is distributed very evenly over the entire specimen and is in the same range as the dial gauge measurements (cf. Table 5). Based on this measurement, the nominal specimen thickness used within the analytical framework in Section 4.5 is reduced to 2.02 mm.

3.3. Data acquisition and postprocessing

The experimental data acquisition and postprocessing used for the determination of phase velocities of Lamb waves is based on Barth et al. [20]. It is characterized by very high accuracy, reproducibility, and automation, which allows the aforementioned consideration of the dispersion relations over a wide frequency range. The method is based on the use of a non-uniform 2d-DFT to evaluate the measurement data for Lamb waves. The successful use of 2d-DFT for this type of applications has been demonstrated before by [21–23].

The evaluation of the measurement data is done in the frequency-wavenumber domain instead of the often used evaluation in the time-space domain. Since at least two modes occur in monofrequency excitation, the frequency-wavenumber domain is well suited for the analysis of the dispersive and multimodal behavior of Lamb waves [11, 57–60]. This also allows the use of multifrequency excitation signals to automate the measurement, which is hardly possible when considered in the time-space domain. An exemplary excitation signal in the time domain is shown in Figure 8 and the transformed signal in the frequency domain in Figure 9. It consists of a Hanning windowed [61] superposition of sinusoidal oscillations and has a temporal length of $T = 80$ ms. The duration can be considered as untypically long for GUW applications, where mostly short bursts or impulse excitations are used. The signal is chosen to ensure a very accurate resolution in the frequency domain. In the first test run, frequencies from 0.25 kHz to 995.25 kHz are excited with a step size of 5 kHz. By repeating the measurement 20 times with excitation signals shifted by 0.25 kHz, a range from $f_{min} = 0.25$ kHz to $f_{max} = 1$ MHz with a step size of $\Delta f = 0.25$ kHz is covered. The excitation signal, described and shown in Figures 8 and 9, is applied in ES1 and is limited to a smaller frequency range and a wider spacing for ES2 due to hardware limitations (cf. Table 1). Table 6 shows the properties of the investigated frequency range for both experimental setups.

Setup	f_{min} [kHz]	f_{max} [MHz]	Δf [kHz]	T [ms]
ES1	0.25	1	0.25	80
ES2	1	0.5	1	125

Table 6: Properties of investigated frequency ranges for ES1 and ES2.

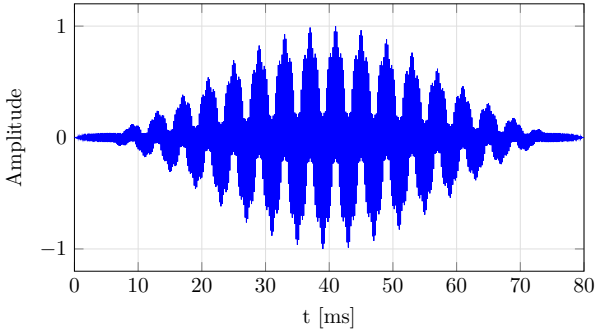


Figure 8: Exemplary representation of a normalized multi-frequency excitation signal in the time domain.

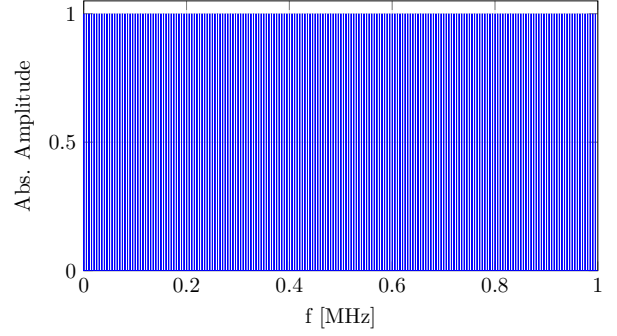


Figure 9: Normalized multifrequency excitation signal from Figure 8 in the frequency domain.

As described in Section 3.1, the required discrete-time velocity data $\mathbf{c}(t, x)$ is generated using a LSV measurement on the specimen's surface at distributed points along a path in the propagation direction x of the waves. The resulting data are processed using a non-uniform 2d-DFT [24]

$$\mathbf{F}(f, \tilde{\nu}) = \sum_{x=0}^n \sum_{t=0}^m (\mathbf{c}(t, x) e^{i2\pi f t}) e^{-i2\pi \tilde{\nu} x}, \quad (13)$$

which converts the data into the frequency-wavenumber domain. Here, f signifies the frequency and $\tilde{\nu}$ the wavenumber. Thereby, the characteristic of Lamb waves is exploited, that they show a sinusoidal behavior in the temporal as well as in the spatial domain [57]. Within the amplitude matrix \mathbf{F} of Equation (13), maxima are detected at given frequency points using a peak-search algorithm. Each resulting frequency-wavenumber pair represents a detected point in the Lamb wave dispersion relation.

In contrast to a direct evaluation of the time signals by e.g. time-of-flight measurements, the advantage of this procedure is a much easier separation of the modes in the frequency-wavenumber domain. In addition, it is possible to specify real phase velocities instead of the often measured group velocities, which is not possible with many other measurement methods without great effort or inaccuracies.

4. Results

In the following, the results of the measurements are compared with each other and with the numerical solution of the analytic framework based on various criteria. It should be noted that the resulting measurement data, as described in Section 3.3 are available in the frequency-wavenumber domain, see Figure 10. However, to ensure better comparability with other publications, all subsequent comparisons are made using the phase velocity c_p as in Figure 11. The relationship required for this is

$$c_p = \frac{f}{\tilde{\nu}}. \quad (14)$$

The only exception is the sorting out of data, see Section 4.1, which is carried out in the frequency-wavenumber domain. This is done because of the linear course of the data for a large range in this domain. In comparison, the course is mostly non-linear in the phase velocity domain.

The following considerations refer to the various specimens and the two measurement setups in this work. Therefore, the measurement labels used are listed in Table 7. Thereby, the measurement data of ES1 and ES2 differ in the range of analyzable frequencies due to the characteristics of the measurement setups described in Section 3.1. Table 8 shows the resulting measurable frequency ranges concerning the experimental setups and the specimen shapes. A more detailed description of the resulting frequency ranges is given in Section 4.1.

The evaluations are structured in different sections. Section 4.1 deals with the sorting out of measurement data and explains the limitation to the measurable frequency range and the detection of erroneous data. Section 4.2 and 4.3 deal with the reproducibility of the measurements. Thereby, the former considers the reproducibility with the same

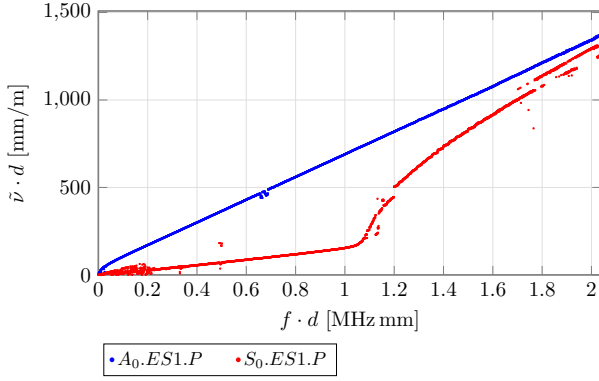


Figure 10: Unsorted sample data in wavenumber representation.

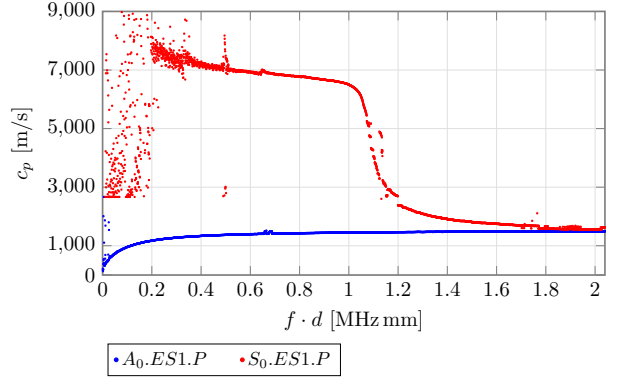


Figure 11: Unsorted sample data in phase velocity representation.

Label	Setup	Type	Run
ES1.P	1	plate	2
ES1.S.MS1	1	strip	1
ES1.S.MS2	1	strip	2
ES2.S	2	strip	1
ES2.P.MS1	2	plate	1
ES2.P.MS2	2	plate	2

Table 7: Description of measurement labels.

Setup	Mode	$(f \cdot d)_{min}$ [kHz mm]	$(f \cdot d)_{max}$ [MHz mm]	$\Delta(f \cdot d)$ [kHz mm]
ES1.S	A_0	43	>2.04	0.51
ES1.S	S_0	443	>2.04	0.51
ES1.P	A_0	43	>2.04	0.51
ES1.P	S_0	443	>2.04	0.51
ES2.S	A_0	43	0.68	2.04
ES2.S	S_0	443	>1.02	2.04
ES2.P	A_0	26	0.96	2.04
ES2.P	S_0	324	>1.02	2.04

Table 8: Frequency-thickness ranges for different experimental setups.

experimental setup while the latter compares the reproducibility with different experimental setups. The influence of the sample width on the measurement results is described in Section 4.4. A conclusion of the considerations is offered in Section 4.5 where a comparison of the measured data with data from the analytical framework is given.

It is to be noted, that the strip specimen is preferably used instead of the plate specimen for the following comparisons. This is due to the continuation of this research, as described in Section 3.2.

4.1. Sorting out data

As expected, the measurements performed partially contain erroneous data due to external disturbances and setup- / or specimen-specific characteristics. To make the data more comparable, the measurement errors are sorted out as exemplarily shown in Figure 12. Two main criteria are used for this:

- All measurement data below and above a specified wavenumber are sorted out. The minimum wavenumber depends on the length of the measuring path on the respective specimen as described in Barth et al. [20]. As a parameter, it is assumed that the measurement length must have at least ten times the length of the

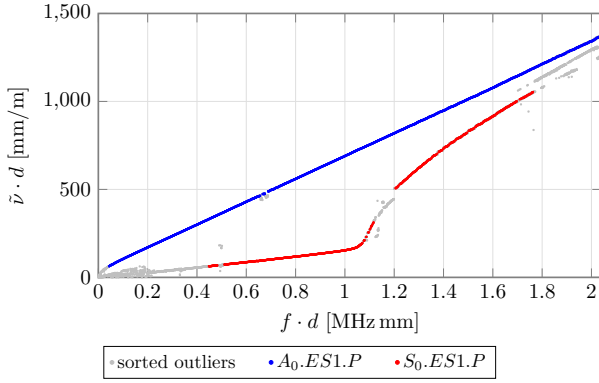


Figure 12: Example for sorting of data for dispersion diagrams in frequency wavenumber representation.

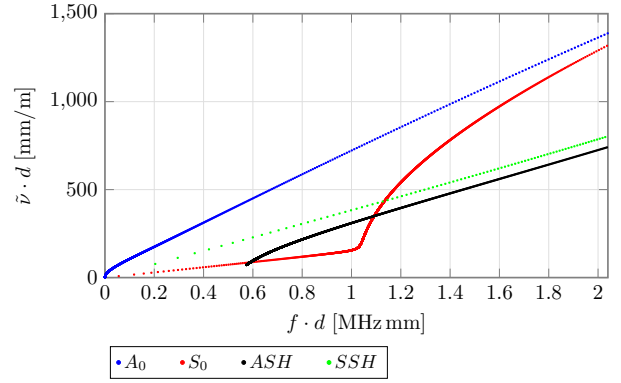


Figure 13: Dispersion diagram from analytical framework including antisymmetric (ASH) and symmetric (SSH) shear horizontal waves. Material parameters from [50].

minimum wavenumber. The maximum wavenumber depends on the distance between successive measuring points. It is assumed that the spatial sampling frequency must be twice as high as the highest wavenumber in the measurement. The resulting minimum and maximum frequencies are shown in Table 8.

- Measurement data is sorted out by generating a fit of the measurement data and determining outliers employing a specified maximum error residual. In the wavenumber domain, a linear fit function can be used for most areas of the measurement data and thus the desired outliers can be detected through a single step. In the frequency ranges in which a linear function is not sufficient, a spline fit is used, which approximates the function step by step and sorts out outliers. For this, the number of measuring points in a certain area is used as weighting for the used spline functions.

Additional reasons for sorting out data because of reappearing measurement deviations are listed below:

- Due to a more inaccurate angular resolution in the LSV at ES2 compared to ES1, data with high wavenumbers had to be removed from consideration since a high scattering of the results occurred in this range. The more prominent occurrence of this effect in the measurement of strip specimen (ES2.S) compared to the ones in the plate specimens (ES2.PMS1 and ES2.PMS2) can be attributed to the shorter measuring path shown in Table 4, since a longer measuring path can compensate for this effect to some degree.
- In the data sorting of the S_0 -mode between 1.1 MHz mm and 1.2 MHz mm a large number of outliers are particularly striking, since they are repeated in all data sets. The deviations can be explained by the occurring shear horizontal wave modes (SH-modes) in this frequency range. Figure 13 shows a representation based on the analytical framework. It can be seen that two SH-modes cross the S_0 -mode in this range. Here, *ASH* and *SSH* stand for an antisymmetric and symmetric shear horizontal wave. This leads to interferences between the wavemodes and causes a disturbance in the evaluation of the S_0 -mode. It should be noted that the frequency range of the perturbation differs slightly between the experimental data in Figure 12 and the analytical data in Figure 13. This is due to a general discrepancy between the analytic and the experimental data, which is discussed in more detail in Section 4.5.
- At frequencies above 1.8 MHz mm the wavenumbers of the two fundamental Lamb modes converge more and more. This results in a superposition of the amplitude maxima in the frequency-wavenumber matrix $\mathbf{F}(f, \tilde{v})$ during the detection and finally in an erroneous shift in the detection of the S_0 -mode. Although the shift happens to both modes it is practically only visible in the S_0 -mode, since the measured out-of-plane velocity has considerably lower amplitudes than in the A_0 -mode.

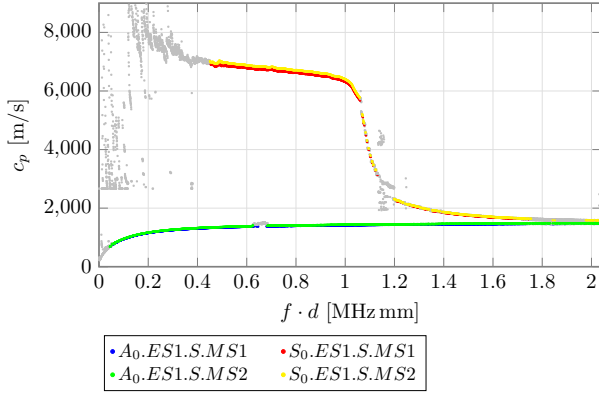


Figure 14: Dispersion diagram for two measurements using the strip specimen with ES1.

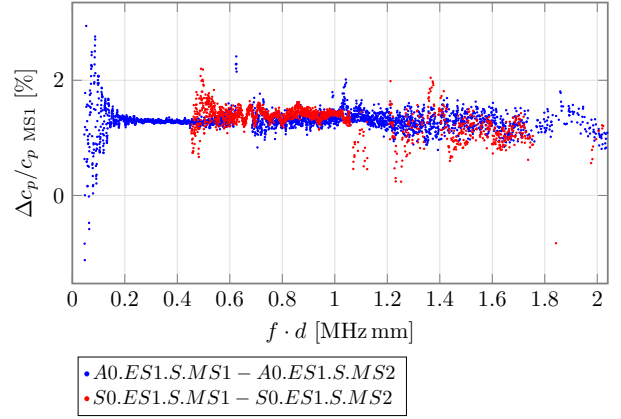


Figure 15: Relative difference between two measurements using the strip specimen with ES1.

4.2. Validating the method's reproducibility with the same experimental setup

In this section, the reproducibility of the measurement results is investigated separately for both experimental setups. This is done to check the method's reliability when generating Lamb wave dispersion diagrams in FML. For each setup, two measurements are performed at different times with the specimen and LSV moved between the two runs, to additionally investigate the reproducibility of setting up the system. Moreover, the method's ability to produce reliable results repeatedly is presented for a strip and a plate specimen, respectively, to show reproducibility in different specimens.

4.2.1. Comparison of strip specimen measurements with ES1

The reproducibility of the dispersion diagram results generated with ES1 is investigated using a strip specimen. The same hardware is used to perform the here shown measurements. Therefore, it is assumed that the method provides reproducible results with consecutive measurements, which is supported by the general curves of the dispersive relation in Figure 14.

The A_0 -mode can be evaluated over a wider frequency range than the S_0 -mode. This is visible in the dispersion diagram by the shorter frequency range with evaluable data points for the S_0 -mode. The limitations for the better detectability of the A_0 -mode are mostly due to smaller wavelengths and a higher out-of-plane amplitude in the investigated frequency range. The minimally detectable wavelengths for the fundamental modes A_0 and S_0 , as described in Section 4.1, correspond to minimal frequencies of 43 kHz mm and 443 kHz mm, respectively.

Figure 15 depicts a criterion to compare the two measurements performed with ES1 by plotting the relative difference and gives a deeper insight into the reproducibility. The results for both fundamental modes show only slight deviations with a maximum error of approx. 3 % and a mean relative difference of less than 1.5 %. The high scattering at the beginning of both detectable frequency ranges is the result of challenging measurement conditions in these frequency regions. As the wavenumbers become smaller with lower frequencies a larger measurement path would be needed for clearer results. As stated above, the A_0 -mode detection is more reliable in the investigated frequency range. This is supported by the wider segment with low scattering. As stated in Section 4.1, wavenumber determination gets complicated for high frequencies for the S_0 -mode due to interference with the high amplitudes of the A_0 -mode that results in wavenumber shifts. This leads to a higher scattering of the S_0 -mode. However, the results are equally convenient.

Considering the results shown here, it can be concluded that the measurements of ES1 show good reproducibility.

4.2.2. Comparison of plate specimen measurements with ES2

The results for the reproducibility investigation of ES2 are presented for a plate specimen. The same hardware is used to conduct the two different measurements. As for ES1, the overall course of the graphs for the two fundamental modes in Figure 16 are nearly the same for both measurements. In contrast to ES1, the maximum investigable frequency is

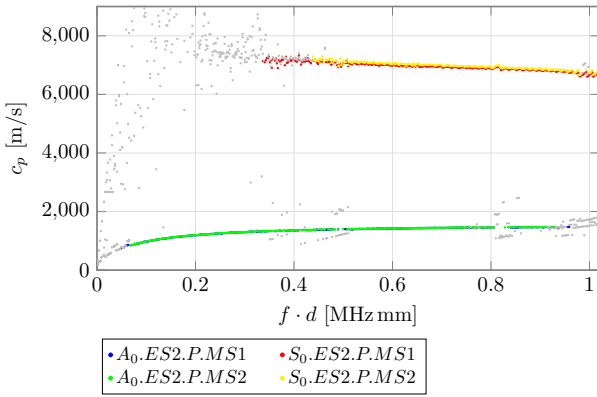


Figure 16: Dispersion diagram for two measurements using the plate specimen with ES2.

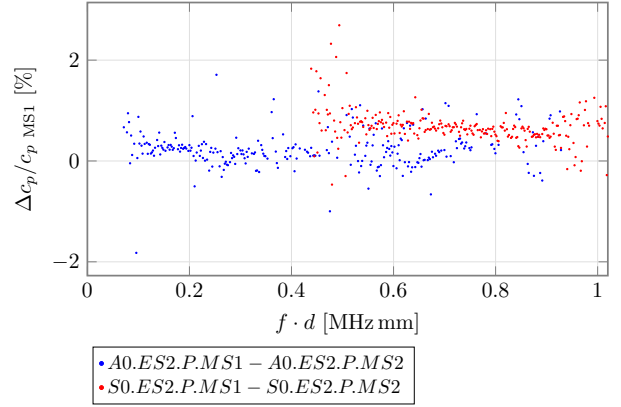


Figure 17: Relative difference between two measurements using the plate specimen with ES2.

limited due to the hardware, as described in Section 4.1. The minimally detectable wavelengths correspond to minimal frequencies of 26 kHz mm and 324 kHz mm for the A_0 - and S_0 -mode, respectively.

Figure 17 depicts the relative difference between the two measurements. The maximum error is approx. 3 %, while the A_0 -mode again shows slightly better reproducibility than the S_0 -mode. The mean relative differences for the A_0 - and S_0 -mode are less than 1 % and 0.5 %, respectively.

In general, ES2 is also suited to generate dispersion diagrams in FML repeatedly. In conclusion, a reliable generation of Lamb wave dispersion diagrams in FML is shown with the presented setups. However, differences in performance between the two setups are to be expected, due to the different hardware equipment. This will be discussed in the following section.

4.3. Validating the measurement results with different experimental setups

Regarding data transfer and comparability in research cooperations, the question arises, whether the presented method is applicable with different experimental setups. The hypothesis is that the method can equally be applied to different setups, while the temporal and spatial resolutions, as well as measurement lengths and durations, define the investigable frequency-thickness product range.

In Section 4.2, the reproducibility of the measurements was shown when using the same experimental setup. In addition, the reproducibility of the measurements using different experimental setups for an identical specimen is investigated by comparing the two measurement setups ES1 and ES2. For better comparability, the strip specimen is selected because of the same measurement path lengths, see Table 4.

As mentioned in Section 3.1, the measurement setups are different with regard to the possible frequency range. Therefore, the comparison is restricted with regard to the frequency limits in Table 8. Besides this, the setups should produce comparable data with slightly clearer results for ES1 thought to the overall qualitatively better measurement devices. This is visible from the smoothness of the data in Figure 18, where the effect is more pronounced in the S_0 -mode due to the consistently lower measured wavenumbers. Otherwise, the graphic shows the expected picture, namely that both measurement setups can clearly show the course of the dispersive relationship. However, as expected, the detection of the A_0 -mode yields significantly better results, which is partly due to the higher wavenumbers as well as the higher out-of-plane amplitudes in comparison to the S_0 -mode. Figure 19 provides a more detailed insight into the differences of the measurements by giving the percentage deviations of the measurements with respect to the measurement of ES1. It can be seen that despite of the different setups, only a small measurement deviation occurs, with a maximum of 4 % and an average difference less than 2 % between the setups. The better evaluability of the A_0 -mode compared to the S_0 -mode is thereby reflected in a significantly smaller scatter of the deviations. In conclusion, the measurements can be clearly reproduced in FML even with different measurement setups, which enables data transfer in research cooperations.

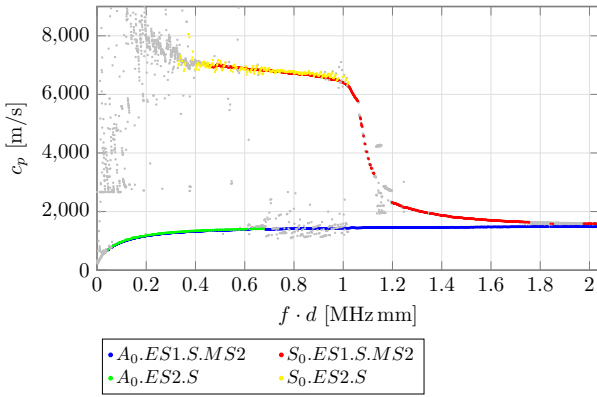


Figure 18: Dispersion diagram of strip measurements with ES1 and ES2.

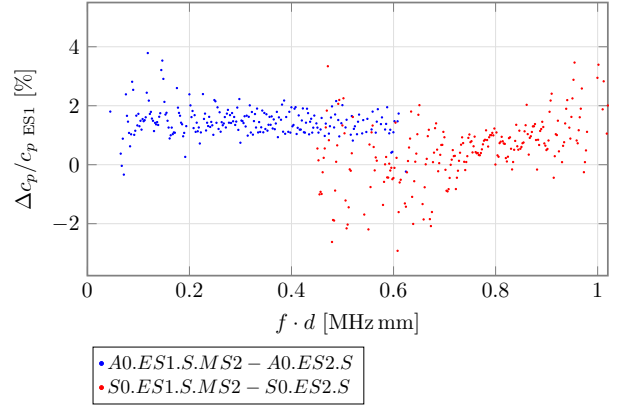


Figure 19: Difference in strip measurements with ES1 and ES2.

4.4. Validating the measurement results with different specimen sizes

As stated above, the aim for future investigations is to mainly use strip specimens for reasons of cost and manufacturing effort as well as space limitations in follow-up research using a tensile test machine. Therefore, this chapter aims at showing the suitability of strip specimens for the presented method of dispersion diagram determination. Generally speaking, specimens that extend as far as possible in the in-plane directions are always advantageous for the determination of Lamb wave propagation phenomena, since reflections and other effects resulting from interactions of the wave with the edges have less influence on the measurement itself. The geometries of the strip and plate specimen under investigation are presented in Table 4. ES1 is chosen for the comparison of the strip specimen to the reference plate since it covers a larger frequency range, see Section 3.1.

Figure 20 shows the dispersion relation of the A_0 - and S_0 -mode for both measurements. Overall, no significant differences occur between the measurement in the plate and the strip specimen. The largest deviations occur in the frequency range of 1-1.2 MHz mm due to the crossing of the SH-modes as discussed in Section 4.1. Therefore, the larger deviations of the two measurements in this region cannot necessarily be attributed to the specimen geometry.

This is supported by the difference plot in Figure 21. It can be seen, that the mean difference between the plate and strip specimens is below 2 %, which is in the same range as the reproducibility of the measurement itself. Therefore, no significant difference between strip and plate specimen for the A_0 -mode can be detected.

As expected, there is more scattering in the difference for the S_0 -mode. However, the absolute difference is less than 5 % and for frequency-thickness products below 1 MHz mm, the mean difference is below 2 %. Although the S_0 -mode difference is slightly higher compared to the previous measurements in this work, it is still considered reasonable.

Generally speaking, the use of a strip specimen instead of a large plate is applicable for the dispersion diagram generation in this setup. The measurements shown indicate that for the considered frequency range the use of strip specimens with a width of 110 mm instead of plates has only small effects on the results. Therefore, the use of strip specimens seems to be very advantageous for cost reasons. It should be noted, that the statements made here about the usability of a strip specimen only refer to the here used specimen width and frequency region. However, the use of even narrower strips might increase the problem of edge reflections significantly.

4.5. Comparison of experimental results and results from analytical framework

In this section, the experimental dispersion relations are compared to numerical data from solving the analytical framework. For simplicity, this solution will be referred to as the analytical solution in the following. The basis for the analytical framework are the presented relations for GUW propagation in laminate structures as described in Section 2.2. The measurements of the strip specimen in ES1 are used for the comparison.

In Figure 22, the analytical solutions are plotted against the measurement of the strip specimen in ES1 for the A_0 -mode. The course of the measured data in the considered frequency range is in good agreement with the analytical values. Figure 23 shows that the percentage deviation between experimental and analytical data is in the single-digit range for both analytic solutions. It can be stated that the parameters out of [50] provide the most suitable solution, with deviations below approx. 5 %.

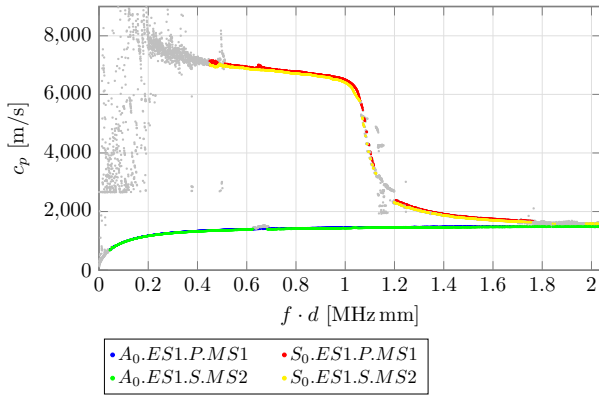


Figure 20: Dispersion diagram of strip and plate measurements.

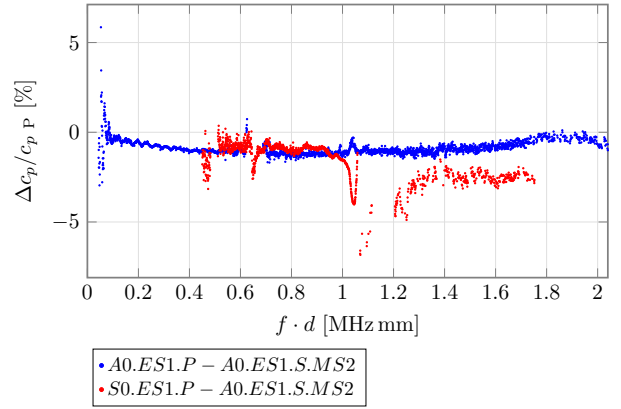


Figure 21: Relative difference between strip and plate measurements.

In Figure 24, the same comparison is shown for the S_0 -mode. Once again, the course of the measurement data is similar to that of the analytic solution. In contrast to the A_0 -mode, larger differences can be found in the S_0 -mode for certain frequency ranges. In the range from 0.9 MHz mm to 1.2 MHz mm, which contains the sharp decrease in phase velocity, a horizontal shift of this drop can be observed. This is also clearly visible in Figure 25, where the maximum relative deviation is approx. between 30 % and 80 % depending on the different material parameter sources. However, the high deviations are mostly due to the shift between the frequency ranges where the sharp decrease in phase velocity occurs. In general, there is good agreement up to approx. 0.9 MHz mm and for frequency-thickness products higher than 1.2 MHz mm.

The comparison of the measured data with the data from the analytical framework shows that the basic course of the dispersion diagrams can be represented. In addition, it can be assumed that an adjustment of the material parameters within a reasonable range would lead to an agreement between the analytical and the experimental data. The investigation of the individual material parameters required for this purpose will be considered in depth in the further course of this research.

Another aspect that was not considered so far is the inherent manufacturing-induced residual stress state in the FML. Interlaminar stresses develop in the CFRP-steel specimen, mainly due to the difference in the coefficients of thermal expansion between steel and CFRP, in combination with the temperatures of up to 180 °C during the manufacturing process. This stress state results in inherent tensile stresses in the metal layers and compressive stresses in the fiber layers after curing. For the layup at hand, the metal layers are subjected to significant tensile stresses that account for up to 20 % of its tensile strength [62]. The residual stresses in the CFRP layers, on the other hand, mean that parameters in the compression range would have to be taken into account for this material. However, these can deviate from those in the tensile range, see [46]. However, this internal stress state is not accounted for in the analytic calculation and might be an additional reason for the deviations between analytical and experimental data. The correlation between internal stress states and wave propagation will be investigated in subsequent studies by the authors.

5. Conclusion

This paper successfully extends the method by Barth et al. [20] of experimentally determining dispersion relations of Lamb waves for isotropic materials, to the use in FML structures. The method has been shown to provide a highly automatable way to detect dispersion relationships of Lamb waves over large frequency ranges with very high accuracy and reproducibility. In addition, the transferability to strip specimen geometries for reasons of material savings and the reproducibility across different measurement setups for future research could also be confirmed.

Thereupon, dispersion diagrams are experimentally determined over wide frequency ranges for FMLs made of carbon fiber-reinforced polymer and steel. The expected dispersion relations are confirmed. A comparison between the experimental data and data from numerical solutions of the analytical framework shows that the differences that occur can be explained by deviations and uncertainties in the material parameters used. Explanatory approaches for

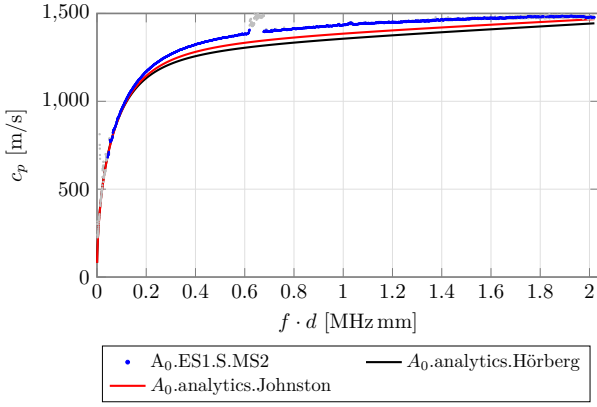


Figure 22: Dispersion diagram of strip measurements and analytic solutions for the A_0 -mode with different material parameters from literature [49, 50].

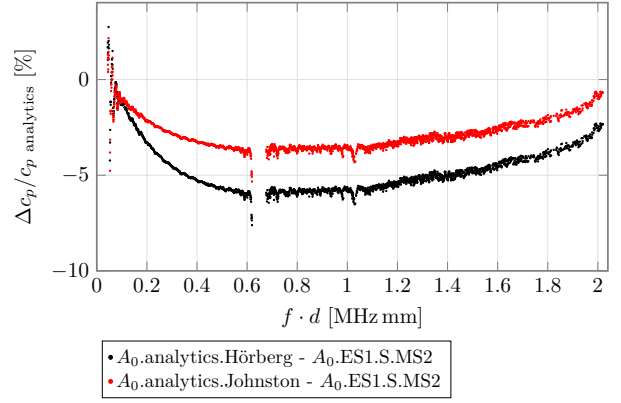


Figure 23: Difference between strip measurements and analytic solution for the A_0 -mode with different material parameters from literature [49, 50].

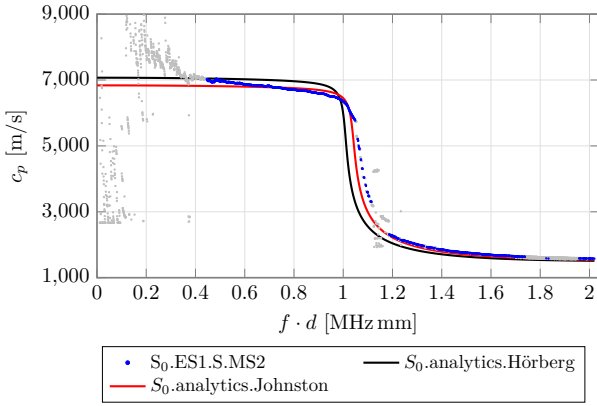


Figure 24: Dispersion diagram of strip measurements and analytic solution for the S_0 -mode with different material parameters from literature [49, 50].

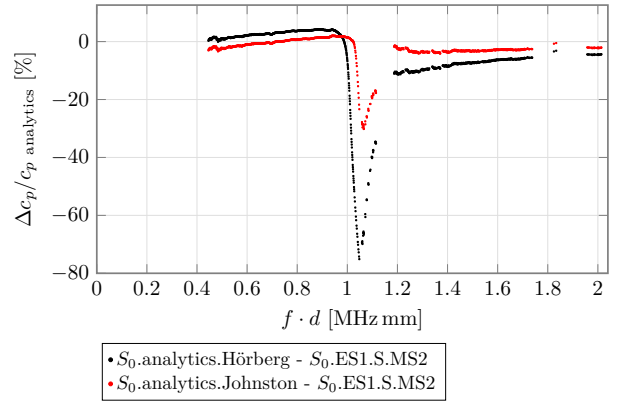


Figure 25: Difference between strip measurements and analytic solution for the S_0 -mode with different material parameters from literature [49, 50].

the deviations are pointed out, and will be addressed in future work. Nevertheless, the results provide a profound basis for the evaluation of Lamb wave based SHM in FML.

In the further course of the research, the measurements are to be extended and supplemented by modeling using FEM. The focus will be on an in-depth investigation of the frequency range where the sharp decrease in phase velocity of the S_0 -mode occurs. Since a possible cause of the discrepancy is suspected due to the presence of residual stresses in the materials induced by the manufacturing process, additional specimens with the same material system but different residual stress states [62] will be compared. This will provide a better insight into the cause of the discrepancy and additionally characterize the influence of manufacturing-related residual stress states on Lamb wave propagation in FML. Furthermore, the influence of variations in the material parameters will be subject to future research.

Acknowledgment

The authors expressly acknowledge the financial support for the research work on this article within the Research Unit 3022 “Ultrasonic Monitoring of Fibre Metal Laminates Using Integrated Sensors” by the German Research Foundation (Deutsche Forschungsgemeinschaft (DFG)).

CRedit authorship contribution statement

Tilman Barth: Conceptualization, Methodology, Investigation, Data Curation, Writing - Original Draft, Writing - Review and Editing, Visualization. **Johannes Wiedemann:** Conceptualization, Methodology, Investigation, Data Curation, Writing - Original Draft, Writing - Review and Editing, Visualization. **Thomas Roloff:** Conceptualization, Methodology, Investigation, Data Curation, Writing - Original Draft, Writing - Review and Editing, Visualization. **Tim Behrens:** Investigation, Data Curation. **Natalie Rauter:** Conceptualization, Methodology, Investigation, Writing - Original Draft, Writing - Review and Editing, Visualization, Funding acquisition, Project administration. **Christian Hühne:** Conceptualization, Writing - Review and Editing, Funding acquisition, Project administration. **Michael Sinapius:** Conceptualization, Writing - Review and Editing, Funding acquisition, Project administration. **Rolf Lammering:** Conceptualization, Writing - Review and Editing, Funding acquisition, Project administration.

Data availability

The publication of the data that support the findings of this study is in progress and will be openly available at the time this study will be published.

References

- [1] A. Vlot, J. W. Gunnink, *Fibre Metal Laminates: An Introduction*, Springer Netherlands, Dordrecht, 2001.
- [2] R. Alderliesten, *Fatigue and fracture of fibre metal laminates*, volume 236 of *Solid mechanics and its applications*, Springer, Cham, 2017.
- [3] G. B. Chai, P. Manikandan, Low velocity impact response of fibre-metal laminates – A review, *Compos Struct* 107 (2014) 363–381. doi:10.1016/j.compstruct.2013.08.003.
- [4] F. Morinière, R. Alderliesten, M. Tooski, R. Benedictus, Damage evolution in GLARE fibre-metal laminate under repeated low-velocity impact tests, *Cent. Eur. J. Eng.* 2 (2012) 1116. doi:10.2478/s13531-012-0019-z.
- [5] J. Bienias, P. Jakubczak, B. Surowska, H. Debski, Experimental and numerical investigations of low-velocity impact behavior of selected fibre metal laminates, *Proceedings of the ECCM16 - 16th European Conference on Composite Materials* 16 (2014).
- [6] A. Güemes, C.-P. Fritzen, D. Balageas, *Struct Health Monit*, ISTE, London and Newport Beach, CA, 2006.
- [7] R. Yan, X. Chen, S. C. Mukhopadhyay, *Struct Health Monit*, volume 26, Springer International Publishing, Cham, 2017.
- [8] R. Lammering, U. Gabbert, M. Sinapius, T. Schuster, P. Wierach (Eds.), *Lamb-Wave Based Structural Health Monitoring in Polymer Composites*, Research Topics in Aerospace, Springer International Publishing, Cham, 2017.
- [9] F.-G. Yuan (Ed.), *Structural health monitoring (SHM) in aerospace structures*, volume number 68 of *Woodhead publishing series in composites science and engineering*, Woodhead Publishing is an imprint of Elsevier, Duxford, UK, 2016.
- [10] V. Giurgiutiu, *Structural health monitoring with piezoelectric wafer active sensors*, Academic Press/Elsevier, Amsterdam, 2008.
- [11] H. Lamb, On waves in an elastic plate, *Proceedings of the Royal Society of London. Series A, Containing Papers of a Mathematical and Physical Character* 93 (1917) 114–128.
- [12] J. L. Rose, *Ultrasonic Guided Waves in Solid Media*, Cambridge Univ. Press, 2014. doi:10.1017/CB09781107273610.
- [13] S. Pant, J. Laliberte, M. Martinez, B. Rocha, Derivation and experimental validation of lamb wave equations for an n-layered anisotropic composite laminate, *Compos Struct* 111 (2014) 566–579. doi:10.1016/j.compstruct.2014.01.034.
- [14] A. Maghsoodi, A. Ohadi, M. Sadighi, H. Amindavar, Damage detection in multilayered fiber-metal laminates using guided-wave phased array, *J Mech Sci Technol* 30 (2016) 2113–2120. doi:10.1007/s12206-016-0418-9.
- [15] A. Muc, M. Barski, A. Stawiarski, M. Chwał, M. Augustyn, Dispersion curves and identification of elastic wave modes for fiber metal laminates, *Compos Struct* 255 (2021). doi:10.1016/j.compstruct.2020.112930.
- [16] S. Tai, F. Kotobuki, L. Wang, A. Mal, Modeling Ultrasonic Elastic Waves in Fiber-Metal Laminate Structures in Presence of Sources and Defects, *J Nondestr Eval Diagn Progn Eng Syst* 3 (2020). doi:10.1115/1.4046946.
- [17] J. Gao, Y. Lyu, M. Zheng, M. Liu, H. Liu, B. Wu, C. He, Modeling guided wave propagation in multi-layered anisotropic composite laminates by state-vector formalism and the legendre polynomials, *Compos Struct* 228 (2019). doi:10.1016/j.compstruct.2019.111319.
- [18] L. Attar, D. Leduc, M. Kettani, M. Predoi, J. Galy, P. Pareige, Detection of the degraded interface in dissymmetrical glued structures using lamb waves, *NDT and E Int* 111 (2020). doi:10.1016/j.ndteint.2019.102213.
- [19] B. Le Crom, M. Castaings, Shear horizontal guided wave modes to infer the shear stiffness of adhesive bond layers, *J Acoust Soc Am* 127 (2010) 2220–2230. doi:10.1121/1.3309441.
- [20] T. Barth, N. Rauter, R. Lammering, Experimental determination of lamb wave dispersion diagrams using 2d fourier transform and laser vibrometry, Preprint at <https://www.researchsquare.com/article/rs-1321459/v1> (2022). doi:10.21203/rs.3.rs-1321459/v1.
- [21] D. Alleyne, P. Cawley, A two-dimensional fourier transform method for the measurement of propagating multimode signals, *J Acoust Soc Am* 89 (1991) 1159–1168. doi:10.1121/1.400530.
- [22] P. Hora, O. Červená, Determination of lamb wave dispersion curves by means of fourier transform, *Appl. Comput. Mech.* 6 (2012) 5–16.
- [23] Z. Su, L. Ye, *Identification of Damage Using Lamb Waves: From Fundamentals to Applications*, volume 48, Springer, London, 2009. doi:10.1007/978-1-84882-784-4.
- [24] R. N. Bracewell, R. N. Bracewell, *The Fourier transform and its applications*, volume 31999, McGraw-Hill New York, 1986.
- [25] T. Sinmazçelik, E. Avcu, M. Ö. Bora, O. Çoban, A review: Fibre metal laminates, background, bonding types and applied test methods, *Mater. Des.* 32 (2011) 3671–3685. doi:10.1016/j.matdes.2011.03.011.

- [26] R. C. Alderliesten, M. Hagenbeek, J. J. Homan, P. A. Hooijmeijer, T. J. de Vries, C. A. J. R. Vermeeren, Fatigue and Damage Tolerance of Glare, *Applied Composite Materials* 10 (2003) 223–242. doi:10.1023/A:1025537818644.
- [27] Y. Boose, E. Kappel, D. Stefaniak, R. Prussak, A. Pototzky, L. Weiß, Phenomenological investigation on crash characteristics of thin layered CFRP-steel laminates, *Int. J. Crashworthiness* 182 (2020) 1–10. doi:10.1080/13588265.2020.1787681.
- [28] A. Fink, P. P. Camanho, J. M. Andrés, E. Pfeiffer, A. Obst, Hybrid CFRP/titanium bolted joints: Performance assessment and application to a spacecraft payload adaptor, *Compos Sci Technol* 70 (2010) 305–317. doi:10.1016/j.compscitech.2009.11.002.
- [29] E. Petersen, D. Stefaniak, C. Hühne, Experimental investigation of load carrying mechanisms and failure phenomena in the transition zone of locally metal reinforced joining areas, *Compos Struct* 182 (2017) 79–90. doi:10.1016/j.compstruct.2017.09.002.
- [30] A. Pototzky, D. Stefaniak, C. Hühne, Potentials of load carrying conductor tracks in new vehicle structures, in: K. Dröder, T. Vietor (Eds.), *Technologies for economical and functional lightweight design, Zukunftstechnologien für den multifunktionalen Leichtbau*, Springer Berlin Heidelberg, Berlin, Heidelberg, 2019, pp. 79–90.
- [31] D. Düring, E. Petersen, D. Stefaniak, C. Hühne, Damage resistance and low-velocity impact behaviour of hybrid composite laminates with multiple thin steel and elastomer layers, *Compos Struct* 238 (2020) 111851. doi:10.1016/j.compstruct.2019.111851.
- [32] R. Lammering, U. Gabbert, M. Sinapius, T. Schuster, P. Wierach, Lamb-Wave Based Structural Health Monitoring in Polymer Composites, Springer International Publishing, 2018. doi:10.1007/978-3-319-49715-0.
- [33] M. Abouhamzeh, Distortions and Residual Stresses of GLARE Induced by Manufacturing, Doctoral dissertation, Delft University of Technology, 2016. doi:10.4233/uuid:1f1b3e5c-72b8-440c-8d98-4b4c82814fb6.
- [34] S. I. Rokhlin, L. Wang, Ultrasonic waves in layered anisotropic media: characterization of multidirectional composites, *Int J Solids Struct* 39 (2002) 5529–5545. doi:10.1016/S0020-7683(02)00500-0.
- [35] M. Lowe, Matrix techniques for modeling ultrasonic waves in multilayered media, *IEEE Trans Ultrason Ferroelectr Freq Control* 42 (1995) 525–542. doi:10.1109/58.393096.
- [36] N. Haskell, The dispersion of surface waves on multilayered media, in: A. Ben-Menahem (Ed.), *Vincit Veritas: A Portrait of the Life and Work of Norman Abraham Haskell, 1905–1970*, American Geophysical Union (AGU), Washington, D. C., 1990, pp. 86–103.
- [37] A. H. Nayfeh, The general problem of elastic wave propagation in multilayered anisotropic media, *J. Acoust. Soc.* 89 (1991) 1521–1531. doi:10.1121/1.400988.
- [38] A. H. Nayfeh, Wave propagation in layered anisotropic media: With applications to composites, volume 39 of *North-Holland series in applied mathematics and mechanics*, Elsevier, Amsterdam and New York, 1995.
- [39] L. Knopff, A matrix method for elastic wave problems, *Bull. Seismol. Soc. Am.* 54 (1964) 431–438. doi:10.1785/BSSA0540010431.
- [40] E. Kausel, Wave propagation in anisotropic layered media, *Int J Numer Methods Eng* 23 (1986) 1567–1578. doi:10.1002/nme.1620230811.
- [41] L. Wang, S. I. Rokhlin, Stable reformulation of transfer matrix method for wave propagation in layered anisotropic media, *Ultrasonics* 39 (2001) 413–424. doi:10.1016/S0041-624X(01)00082-8.
- [42] S. I. Rokhlin, L. Wang, Stable recursive algorithm for elastic wave propagation in layered anisotropic media: Stiffness matrix method, *J Acoust Soc Am* 112 (2002) 822. doi:10.1121/1.1497365.
- [43] M. Neumann, B. Hennings, R. Lammering, Identification and avoidance of systematic measurement errors in lamb wave observation with one-dimensional scanning laser vibrometry, *Strain* 49 (2013) 95–101. doi:10.1111/str.12015.
- [44] V. Thierry, O. Mesnil, D. Chronopoulos, Experimental and numerical determination of the wave dispersion characteristics of complex 3D woven composites, *Ultrasonics* 103 (2020) 106068. doi:10.1016/j.ultras.2020.106068.
- [45] C. Shannon, Communication in the presence of noise, *Proceedings of the IRE* 37 (1949) 10–21. doi:10.1109/jrproc.1949.232969.
- [46] National Institute for Aviation Research - Wichita State University, Hexcel 8552 AS4 Unidirectional Prepreg at 190 gsm & 35% RC Qualification Material Property Data Report, 2011. URL: <https://www.wichita.edu/research/NIAR/Research/hexcel-8552/AS4-Unitape-2.pdf>.
- [47] Hexcel Corporation, Product data sheet - HexPly 8552, 2016. URL: https://www.hexcel.com/user_area/content_media/raw/HexPly_8552_eu_DataSheet.pdf.
- [48] T. Garstka, Separation of process induced distortions in curved composite laminates, Ph.D. thesis, The University of Bristol, Bristol, 2005.
- [49] E. Hörberg, T. Nyman, M. Åkermo, S. Hallström, Thickness effect on spring-in of prepreg composite L-profiles – An experimental study, *Compos Struct* 209 (2019) 499–507. doi:10.1016/j.compstruct.2018.10.090.
- [50] A. A. Johnston, An integrated model of the development of process-induced deformation in autoclave processing of composite structures, Ph.D. thesis, University of British Columbia, 1997. URL: <https://open.library.ubc.ca/collections/ubctheses/831/items/1.0088805>. doi:http://dx.doi.org/10.14288/1.0088805.
- [51] DIN Deutsches Institut für Normung e.V., *Federband aus nichtrostenden Stählen: Technische Lieferbedingungen*, 2003.
- [52] D. Stefaniak, E. Kappel, B. Kolesnikov, C. Hühne, Improving the mechanical performance of unidirectional CFRP by metal-hybridization, *Proceedings of the ECCM15 - 15th European Conference on Composite Materials* 15 (2012).
- [53] 3M Aerospace and Commercial Transportation Division, 3M™ Surface Pre-Treatment AC-130-2, 2015. URL: <https://multimedia.3m.com/mws/media/10638340/3m-surface-pre-treatment-ac-130-2-application-guide.pdf>.
- [54] K. Y. Blohowski, J. H. Osborne, K. A. Krienke, Patent: Surface pretreatment of metals to activate the surface for sol-gel coating, 1999. U.S. Patent No. US5869140A.
- [55] D. Stefaniak, Improving residual strength of unidirectionally reinforced plastic laminates by metal layering, Ph.D. thesis, Technische Universität Carola-Wilhelmina zu Braunschweig, 2017.
- [56] Henkel Corporation, Technical Data Sheet - Loctite EA9466, 2019. URL: <http://tds.henkel.com/tds5/Studio/ShowPDF/243%20NEW-EN?pid=EA%209466&format=MTR&subformat=REAC&language=EN&plant=WERCs>.
- [57] K. Graff, *Wave Motion in Elastic Solids*, Dover Books on Physics, Dover Publications, 2012.
- [58] J. D. Achenbach, *Wave propagation in elastic solids*, North-Holland Pub. Co.; American Elsevier Pub. Co Amsterdam, New York, 1973.

- [59] W. H. Prosser, M. D. Seale, B. T. Smith, Time-frequency analysis of the dispersion of lamb modes, *J. Acoust. Soc.* 105 (1999) 2669—2676. doi:10.1121/1.426883.
- [60] W. J. Staszewski, B. C. Lee, L. Mallet, F. Scarpa, Structural health monitoring using scanning laser vibrometry: I. lamb wave sensing, *Smart Mater Struct* 13 (2004) 251–260. doi:10.1088/0964-1726/13/2/002.
- [61] R. B. Blackman, J. W. Tukey, *The Measurement of Power Spectra, from the Point of View of Communications Engineering*, Dover Publications, 1959.
- [62] J. Wiedemann, R. Prussak, E. Kappel, C. Hühne, In-situ quantification of manufacturing-induced strains in fiber metal laminates with strain gages, *Preprint* (2022). doi:10.24355/dbbs.084-202203010939-0.